

Designing quantum many-body matter with conditional generative adversarial networks

Rouven Koch¹ and Jose L. Lado¹

¹*Department of Applied Physics, Aalto University, 00076 Aalto, Espoo, Finland*

(Dated: February 2, 2022)

The computation of dynamical correlators of quantum many-body systems represents an open critical challenge in condensed matter physics. While powerful methodologies have risen in recent years, covering the full parameter space remains unfeasible for most many-body systems with a complex configuration space. Here we demonstrate that conditional Generative Adversarial Networks (GANs) allow simulating the full parameter space of several many-body systems, accounting both for controlled parameters, and stochastic disorder effects. After training with a restricted set of noisy many-body calculations, the conditional GAN algorithm provides the whole dynamical excitation spectra for a Hamiltonian instantly and with an accuracy analogous to the exact calculation. We further demonstrate how the trained conditional GAN automatically provides a powerful method for Hamiltonian learning from its dynamical excitations, and to flag non-physical systems via outlier detection. Our methodology puts forward generative adversarial learning as a powerful technique to explore complex many-body phenomena, providing a starting point to design large-scale quantum many-body matter.

I. INTRODUCTION

The dynamical properties of quantum many-body models remain one of the critical problems in condensed matter physics, lying at the heart of problems ranging from correlated superconductivity [1] to quantum spin liquid physics [2, 3]. Even with the appearance of powerful new methodologies in the last years [4, 5], tackling specific regimes of quantum many-body models is an outstanding problem [6, 7] and covering the full parameter space of a many-body Hamiltonian quickly is a nearly unfeasible task. This huge complexity is not a feature alone of quantum many-body physics, but it is also well known in many problems of image, voice, and video recognition [8–10]. In these fields, a new family of algorithms known as *Generative Adversarial Networks* (GANs) [11] has allowed to tackle some of those intractable problems with high accuracy [12–14].

While supervised and unsupervised learning has been widely applied to quantum problems [15–27], generative adversarial learning remains relatively unexplored [28–30]. The advantages of GANs over simple (supervised or unsupervised) *neural network* (NN) models are the ability of learning underlying distributions of complex data set (e.g., images) and the generation of new samples with the same statistics by only using input noise (and additional conditional parameters) [31, 32]. The generated output is of such high accuracy, e.g., photo-realistic images, that can not be achieved similarly with other generative models [33]. Moreover, GANs naturally incorporate noise in the generative network architecture which enables to account for both uncertainty and diversity in the model. This includes *multi-modal learning* where one input can correspond to several correct outputs which can not be achieved by classical machine learning algorithms which generally learn a one-to-one mapping [34].

Here we show how *conditional* GANs (cGANs) allow

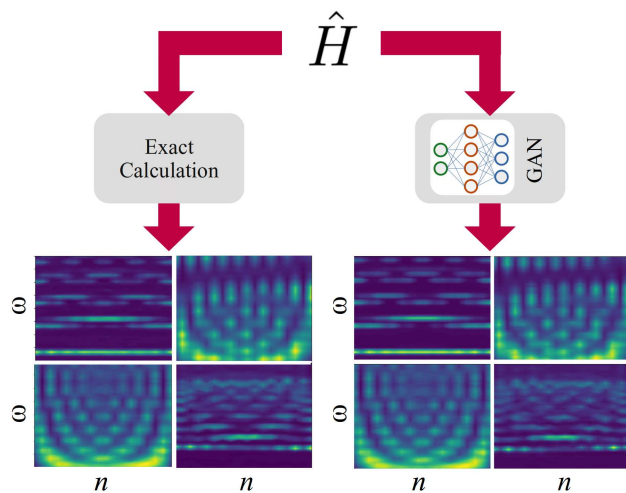


FIG. 1. Comparison of the dynamical correlator computed with an exact many-body formalism (left) and a trained conditional generative adversarial neural network (right). After training, the cGAN allows generating many-body spin correlators of analogous quality to the many-body formalism in the whole parameter space. The trained cGAN accounts simultaneously both for controlled Hamiltonian parameters and hidden disorder effects.

simulating dynamical excitations of many-body Hamiltonians and furthermore provide efficient Hamiltonian learning and outlier detection. Taking as training examples a finite set of noisy many-body dynamical calculations, we demonstrate that the conditional GAN quickly learns to generate dynamical results for the whole parameter space (as illustrated in Fig. 1). Once the GANs are trained, the computational and generalization power of GANs over traditional methods comes into play: even to simulate new many-body Hamiltonians of big system size, the outputs of the GAN are almost instan-

taneous and with an accuracy rivaling the exact calculations, enabling a detailed mapping of complex many-body systems without the need to calculate every parameter combination. Besides realizing a powerful simulator, the trained GAN automatically provides two additional features by exploiting the trained discriminator. First, the parameters of the Hamiltonian can be directly inferred from the simulated dynamical data by using the cGAN discriminator, a methodology providing a cGAN-based Hamiltonian learning algorithm. Second, the trained discriminator allows detecting non-physical results such as those stemming from wrongly computed dynamical many-body systems. Our work provides a first step towards designing quantum many-body matter with deep generative models, opening a pathway to address complex quantum many-body landscapes and ultimately combining theoretical and experimental data.

The manuscript is organized as follows. Sec. II introduces the general concept of cGANs and the quantum many-body methodology for computing dynamical correlators with tensor networks. As a first demonstration, Sec. III exemplifies our cGAN methodology for a family of single-particle models. Sec. IV demonstrates the cGAN methodology for three families of quantum many-body systems, including a gapless many-body model featuring spinons, a model with topological order, and a fermionic Hubbard model. Sec. V demonstrates how the trained cGAN provides both a methodology for Hamiltonian learning and outlier detection. Finally, Sec. VI summarizes our conclusions. Information about the GAN architecture and training data generation are given in Appendix A and B.

II. GENERATIVE ADVERSARIAL NETWORKS AND DYNAMICAL CORRELATORS

A. Generative Adversarial Networks

Generative Adversarial Networks were proposed in 2014 as deep generative models in the context of unsupervised Machine Learning (ML) [11]. They are generally built by combining two neural networks, the generator G and discriminator D , which are competing in a min-max game against each other. This allows the generator to become very accurate in mapping from a latent space vector \mathbf{z} (i.e., a random input vector) to the data distribution of the real images. The generator network tries to trick the discriminator which has the job of distinguishing between real and generated images. During the training process, the parameters of both networks get updated simultaneously, minimizing the terms related to the generator $\log[1 - D(G(\mathbf{z}))]$ and discriminator $\log[D(x)]$ which are part of the GAN value function

$$\min_G \max_D V(D, G) = \mathbb{E}_{x \sim p_{\text{data}}(\mathbf{x})} [\log D(\mathbf{x})] + \mathbb{E}_{z \sim p_z(\mathbf{z})} [\log (1 - D(G(\mathbf{z})))] . \quad (1)$$

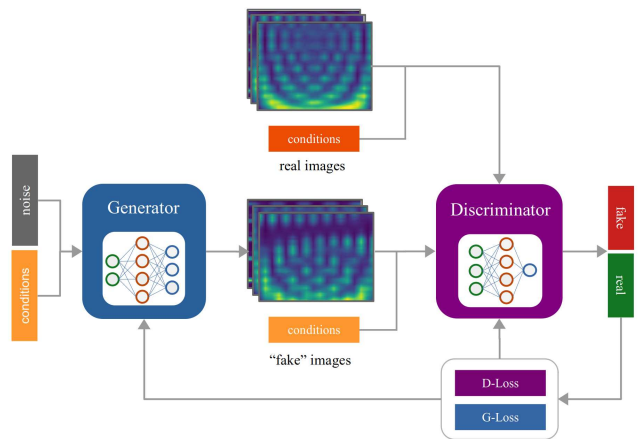


FIG. 2. Illustration of the cGAN architecture used in this work. The cGAN consists of two deep neural networks, the generator G and discriminator D , playing a min-max game against each other. The generator learns the (labeled) data distribution from the real images and the discriminator tries to distinguish between real and generated images. The network parameters are updated during the training via the D-Loss and G-Loss.

The input data \mathbf{x} contains the information of the real images, p_{data} is the distribution of the input images which we want to learn, and p_z is the (normal) distribution of the latent space. During the training, the parameters of the generator (discriminator) are updated in order to minimize (maximize) the expectation values of the value function $V(D, G)$.

Applications of GANs in computer science tasks usually include the generation of images including convolutional neural networks and have shown great success in the applications of image generation by using random inputs [31, 35, 36]. These random inputs, however, inhibit us from controlling the output of the algorithm. An extension to the usual GAN are cGANs which give additional information to the neural networks in order to gain some control over the output of the algorithm without losing the generative power of this method [37]. Some applications include, e.g., image-to-image translation [12] or image editing [8, 32, 38, 39]. The computational power of (conditional) GANs has already found its way to physics, starting in high energy physics for the simulation of 2D particle jet images [40] and 3D particle showers [41], cosmology for emulations of cosmological maps [42], and in selected problems of quantum and condensed matter physics including the simulation of correlated Quantum Walk [28] and to simulate 2D Ising model near the critical temperature [29]. Recently, conditional GANs have also been successfully applied for quantum state tomography and the reconstruction of density matrices [30].

In particular, conditional GANs allow for the incorporation of prior knowledge about a system and simultaneously account for a degree of diverse randomness in the

output. This architecture corresponds to cGANs which have a vector of labels (\mathbf{y}) in addition to the training data as input of the generator and discriminator. In the specific case of our manuscript, we consider conditional labels that are given by the different energy scales of a general Hamiltonian. Figure 2 shows the general architecture of the cGAN used in this work. This architecture is inspired by conventional GANs, yet with the key difference that conditional parameters are included as input for the generator and discriminator (shown in orange). The value function is also very similar to the one of Eq. 1 [37]

$$\min_G \max_D V(D, G) = \mathbb{E}_{\mathbf{x} \sim p_{\text{data}}(\mathbf{x})} [\log D(\mathbf{x}|\mathbf{y})] + \mathbb{E}_{\mathbf{z} \sim p_z(\mathbf{z})} [\log (1 - D(G(\mathbf{z}|\mathbf{y})))] \quad (2)$$

with conditional constraints \mathbf{y} in the input of the discriminator and generator in their corresponding term in the value function. In the case of image generation, the auxiliary labels of the cGAN have discrete class values. In our case, we are using continuous labels which allows us to cover the full parameter space of a given Hamiltonian with a continuous cGAN. In contrast to conventional GANs, we now have the ability to simulate many-body systems with conditional parameters in the Hamiltonian.

B. Dynamical correlators with tensor-networks

Here we summarize the many-body method used to generate the training data. We will be interested in computing the dynamical correlator of a many-body Hamiltonian, taking the form

$$\chi(\omega) = \langle GS | \hat{A} \delta(\omega - \hat{H} + E_0) \hat{B} | GS \rangle \quad (3)$$

where $\hat{A}, \hat{B}, \hat{H}$ are many-body operators and $|GS\rangle$ is the many-body ground state. This spectral function corresponds to the dynamical spin structure factor for a spin system and the electronic many-body density of states for an electronic system. The dynamical correlator is computed using the tensor-network kernel polynomial algorithm [43–50]. The many-body states and Hamiltonians are represented in terms of a tensor-network, using the matrix-product state formalism [51–53], the ground state is computed with the density-matrix renormalization group algorithm [4], and the Hamiltonian is scaled to the interval $(-1, 1)$ to perform the Chebyshev expansion [43]. The scaled Hamiltonian is denoted as \bar{H} , and its scaled spectral function as $\bar{\chi}$, taking the form

$$\bar{\chi}(x) = \frac{1}{\pi \sqrt{1-x^2}} \left[\alpha_0 + 2 \sum_{n=1}^{\infty} \alpha_n T_n(x) \right] \quad (4)$$

with $T_n(x)$ the Chebyshev polynomials and α_n the coefficients of the expansion computed recursively, and including the Jackson Kernel [54]. Finally, we note that

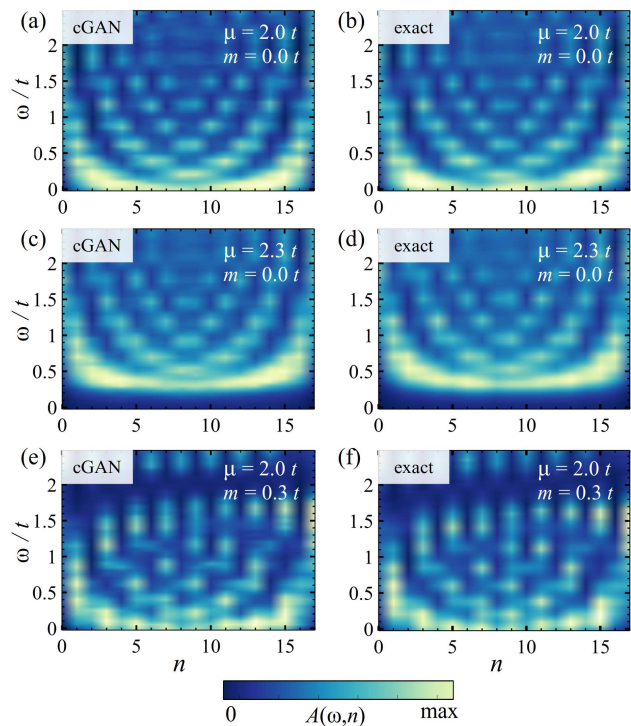


FIG. 3. Real space DOS of a one-dimensional tight-binding system of length $n = 18$ generated with the cGAN (a,c,e) in comparison with the exact tight-binding calculations (b,d,f). The x-axis labels the site, the y-axis the frequency, and the z-axis the (local) DOS (Eq. 6). Shown are 3 combinations of the conditional parameters (μ, m) in (a,b), (c,d) and (e,f), as defined in Eq. 5.

while we focus here on the tensor-network representation of the states, an analogous procedure can be performed with neural-network quantum states [55].

III. SINGLE-PARTICLE SYSTEMS

While ultimately we will explore our generative algorithm for a quantum many-body system, it is instructive to first explore its applicability for a family of single-particle models that can easily be solved. As the first proof of concept, we test our cGAN for a one-dimensional single-particle tight-binding system. The Hamiltonian in second quantization of these systems is given by

$$H(\mu, m) = t \sum_n c_n^\dagger c_{n+1} + \text{h.c.} + \mu \sum_n c_n^\dagger c_n + m \sum_n (-1)^n c_n^\dagger c_n + \sum_n v_n c_n^\dagger c_n, \quad (5)$$

with the hopping t , v_n random onsite energies, and μ as chemical potential. The additional fourth term in the equation introduces a site imbalance with magnitude m and defines together with the chemical potential the

conditional parameter space of our Hamiltonian. The onsite energies v_n are chosen randomly in the interval $v_n \in [-0.1, 0.1]t$ to introduce the randomness in the training data of the cGAN. This randomness emulates potential hidden variables in the model, small fluctuations associated with the theoretical methodology, and would allow mimicking additional perturbations which could be present in potential future experimental data and were not accounted for by the theoretical model. We computed 4000 real systems and extended the training set with the data-enhancement method presented in App. B to 32 000 examples.[56] This training set size is therefore in the order of the MNIST data set of handwritten digits [57]. The parameters μ and m are the conditional parameter of the GAN and are defined in the intervals $\mu \in [1.7, 2.3]t$ and $m \in [-0.3, 0.3]t$.

The idea is to train the generator to map from (μ, m) to the (local) density of states $A(\omega, n)$ (DOS) which is defined as

$$A(\omega, n) = \langle n | \delta(\omega - H) | n \rangle \quad (6)$$

where \mathcal{H} is the tight binding matrix defined by Eq. 5, and δ the Dirac delta function. Figure 3 shows the value of the DOS (z-axis) depending on the site (x-axis) and frequency (y-axis). We show the spatial-resolved DOS for 3 different conditional parameter combinations (μ, m) and compare the simulations of the cGAN in Fig. 3 (a,c,e) with the exact calculations in Fig. 3 (b,d,f). As observed in the figure, there is no visual difference between the real and generated DOS for each of the three parameter choices, a feature observed for generic examples. In particular, in Fig. 3 (c,d), the increase of μ gives rise to a frequency shift of $0.3t$ compared to Fig. 3 (a,b), which is very well captured by the generated DOS of the cGAN in (c). Similar results can be seen in Fig. 3 (e,d), where the increased m -parameter induces a site imbalance between odd and even sites in the chain. In conclusion, the simulations of the algorithm capture the effects of both conditional parameters on the DOS with high accuracy and in arbitrary magnitude. The trained generator is able to generate new systems with arbitrary parameter choice of (μ, m) in the boundaries of the training interval, and even slightly outside, almost instantaneous with very high precision. In the next section, the same algorithm is applied to three different many-body systems which are computational more demanding than the single-particle system which can be seen as proof of principle.

IV. MANY-BODY SYSTEMS

In contrast to the single-particle case in the previous section, calculations of many-body systems with high accuracy are computationally much more demanding. This affects the training of the cGAN because creating an arbitrary large training set becomes one of the major bottlenecks. The idea is to use the minimal amount of data to train the network accurately and use methods of data

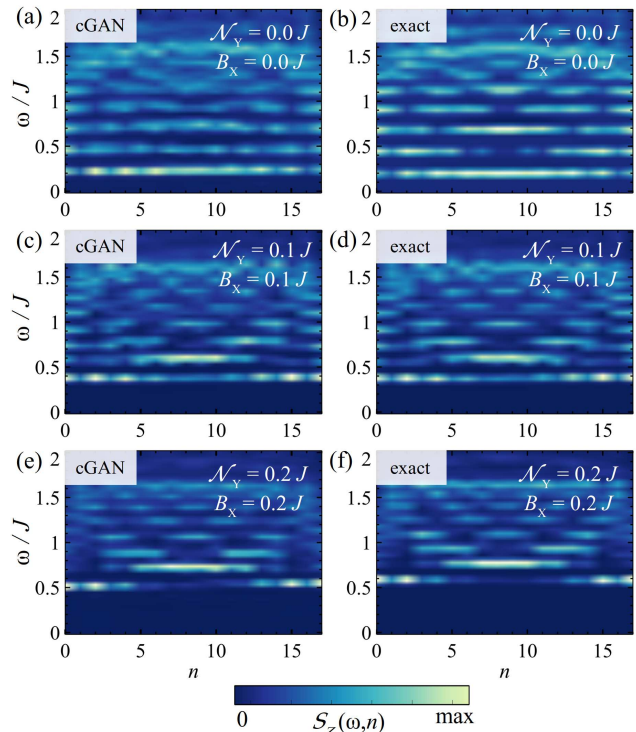


FIG. 4. Real space S^z spin correlators of a one-dimensional $S = 1/2$ -spin chain of length $n = 18$ generated with the cGAN (a,c,e) in comparison with exact tensor-network calculations (b,d,f). The x-axis labels the site, the y-axis the frequency, and the z-axis the full spin correlator (Eq. 8). Shown are 3 combinations of the conditional parameters (\mathcal{N}_y, B_x) in (a,b), (c,d), and (e,f), defined in Eq. 7.

enhancements to enlarge the training set (see App. B). This minimizes the computational effort and takes full advantage of the generative power of this algorithm. In this section, we test our cGAN algorithm for three different one-dimensional many-body systems including a $S = 1/2$ -chain, a topologically non-trivial $S = 1$ system, and a doped Hubbard model [58].

A. Gapless many-body $S = 1/2$ spin model

We start with the simplest many-body system we studied, an interacting $S = 1/2$ Heisenberg model realizing a quantum-disordered ground state. The Hamiltonian for the one-dimensional $S = 1/2$ system is given by

$$H(\mathcal{N}_y, B_x) = J \sum_n \mathbf{S}_n \cdot \mathbf{S}_{n+1} + \mathcal{N}_y \sum_n (-1)^n S_n^x + B_x \sum_n S_n^y + \sum_n (\xi_n^x S_n^x + \xi_n^y S_n^y) \quad (7)$$

with $\mathbf{S}_n = (S_n^x, S_n^y, S_n^z)$ the $S = 1/2$ many-body spin operators. The parameter J denotes the Heisenberg exchange coupling, \mathcal{N}_y a local alternating Neel magnetic field in the y -direction, and B_x a uniform Zeeman field

in the x -direction. In the absence of Neel, Zeeman, and disorder fields, this model realizes a well-understood isotropic Heisenberg model. In this limit, the system features gapless $S = 1/2$ spinon excitations [59] hosting a spin-singlet ground state with local zero magnetization in the thermodynamic limit [60] and can be analytically solved via Bethe ansatz [61]. In the presence of finite Neel and Zeeman terms, the ground state of the system develops a finite order in the x and y directions $\langle S_n^x \rangle \neq 0$, $\langle S_n^y \rangle \neq 0$, yet hosting a zero local order in the z -direction $\langle S_n^z \rangle = 0$. For our cGAN, the parameters \mathcal{N}_y and B_x are the conditional parameters, defined in the intervals $\mathcal{N}_y \in [0.0, 0.2]J$ and $B_x \in [0.0, 0.2]J$, and ξ^x and ξ^y are introducing randomness (up to $0.05J$) to the training data generation.

We now focus on the spin excitations in real space computed with the dynamical spin correlator defined as

$$S_z(\omega, n) = \langle GS | S_n^z \delta(\omega - H + E_{GS}) S_n^z | GS \rangle \quad (8)$$

where S_n^z is the local spin operator in site n , $|GS\rangle$ the many-body ground state, and E_{GS} the ground state energy. The previous correlator directly probes many-body spin excitations in the spin chain and can be directly measured experimentally in real space [62] using inelastic spectroscopy [63–65] and electrically-driven paramagnetic resonance with scanning tunneling microscopy [66–70]. We train the cGAN to map from the conditional parameters to the correlator in real space $(\mathcal{N}_y, B_x) \rightarrow \mathcal{S}$. For the training we used 2250 many-body calculations with arbitrary conditional parameter combinations and used data-enhancement methods (shown in App. B) to increase the training set size to 36 000.

The results for the $S = 1/2$ system for 3 different parameter combinations are shown in Fig. 4 (a,b), Fig. 4 (c,d) and Fig. 4 (e,f). We compare the simulated systems in Fig. 4 (a,c,e) with the real many-body calculations in Fig. 4 (d,e,f). The parameter combinations cover different areas of the parameter space of the Hamiltonian of Eq. 7 and are chosen randomly. The cGAN simulates the spin excitations in z -direction with high accuracy and captures the important features including the spatial profile of the many-body modes in the full frequency range. Differences for the 3 parameter combinations occur in the form of a shift of the lowest excitation and the location and number of higher many-body modes. In Fig. 4 (a,b) the lowest excitation is at $0.25J$ which is captured well in the generated system in (a). Especially for $\mathcal{N}_y = 0.1J$ and $B_x = 0.1J$ the simulation (Fig. 4 (c)) is very close to the real spectrum (Fig. 4 (d)) comparing the energy onset of the excitation at around $0.5t$ as well as the relative magnitudes of higher many-body excitations. The same applies to the third parameter combination of $\mathcal{N}_y = 0.2J$ and $B_x = 0.2J$ in Fig. 4 (e) and Fig. 4 (f), respectively. Differences between the simulations and real images can be related to, first, the induced noise up to $0.05J$ and the random sampling of the cGAN from this noise distribution, i.e., every system generated by the cGAN shows small but observable differences. The second source of

error is connected with the small amount of real training data which implies that for each arbitrary combination of conditional parameters only a small number of training examples exists (in the vicinity of the parameter space). Despite these features, the results for these values and arbitrary parameter combinations are very precise considering the comparatively small amount of training data in terms of GANs (we used only 2250 real data points compared the e.g. the MNIST data set of 60 000 examples) and the instantaneous generation of the spectra.

B. Interacting many-body system with topological order

The one-dimensional $S = 1$ spin chain is a topological non-trivial system that shows spin fractionalization in form of excitations of $S = 1/2$ spins below the bulk gap on the edges of the chain [71–75]. This model represents one of the simplest examples of many-body fractionalization stemming from topological order. This system shows robust topological edge modes, resilient to perturbations that do not break the spin rotational symmetry of the model [73, 76], and has been realized both in natural compounds [77] and artificial designer platforms [78]. In stark contrast with the model of the previous section, the dynamical spectra of this topological model show persistent edge excitations, together with bulk modes, providing a substantially different qualitative behavior.

The Hamiltonian of the spin $S = 1$ Heisenberg model we consider is given by

$$\begin{aligned} H(\Delta_J, J_2) = & J \sum_n \mathbf{S}_n \cdot \mathbf{S}_{n+1} + J_2 \sum_n \mathbf{S}_n \cdot \mathbf{S}_{n+2} \\ & + \Delta_J \sum_n (-1)^n \mathbf{S}_n \cdot \mathbf{S}_{n+1} \\ & + \sum_n \xi_n^J \mathbf{S}_n \cdot \mathbf{S}_{n+1} + \sum_n \xi_n^{J_2} \mathbf{S}_n \cdot \mathbf{S}_{n+2} \end{aligned} \quad (9)$$

with $\mathbf{S}_n = (S_n^x, S_n^y, S_n^z)$ the many-body spin operators for $S = 1$. In comparison to Eq. 7, we have now chosen the dimerization of the nearest-neighbor exchange (Δ_J) and second-nearest-neighbor exchange (J_2) as conditional parameters. We note that external magnetic fields would break the protection of the low-energy topological excitations of the fractionalized spins of this system which we want to study, and, therefore, are not included. In turn, we introduce two noise terms in the model which respect the topological class, in particular spatially-dependent fluctuation in the exchange ξ_n^J and second-neighbor exchange $\xi_n^{J_2}$. Those two random fluctuations would account for small spatial inhomogeneities of the system in an experimental realization [77, 78] stemming from local defects. The conditional parameters are defined in the intervals $J_2 \in [-0.2, 0.2]J$ and $\Delta_J \in [-0.2, 0.2]J$, and ξ_n^J and $\xi_n^{J_2}$ are introducing randomness up to $0.05J$. In this case, the cGAN learns a mapping from (J_2, Δ_J) to

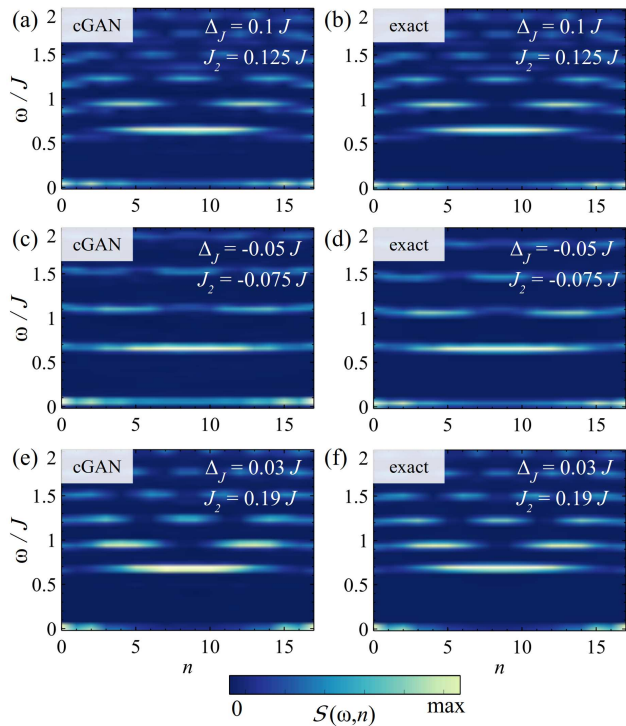


FIG. 5. Real space S^z spin correlators of a one-dimensional $S = 1$ -spin chain of length $n = 18$ generated with the cGAN (a,c,e) in comparison with exact tensor-network calculations (b,d,f). The x-axis labels the site, the y-axis the frequency, and the z-axis the full spin correlator (Eq. 10). Shown are 3 combinations of the conditional parameters (Δ_J, J_2) in (a,b), (c,d), and (e,f), defined in Eq. 9.

the full spin correlator

$$\mathcal{S}(\omega, n) = \sum_{\alpha} \langle GS | S_n^{\alpha} \delta(\omega - H + E_{GS}) S_n^{\alpha} | GS \rangle \quad (10)$$

that denotes spin excitations in real space. It is worth noting that, due to the spin isotropy of Eq. 9, the correlator of Eq. 10 is proportional to Eq. 8 for the considered $S = 1$ model, and can be measured analogously in engineered spin chains with scanning tunneling probes [62–70].

In Fig. 5 we have chosen three arbitrary parameter combinations in order to compare the real spin excitations in Fig. 5 (b,d,f) with the simulations of the cGAN in Fig. 5 (a,c,e). For all parameter combinations, the fractionalized $S = 1/2$ excitations emerge at the edges of the chain close to $\omega = 0 J$ and are mostly not affected by variation of the first and second-neighbor interactions. Due to finite size effects, the fractionalized excitations have a non-zero magnitude even in the middle of the chain for all parameter combinations, due to the dependence of the topological gap on the parameters J_2 and Δ_J . This effect is, however, of different magnitude for different choices of J_2 and Δ_J . In case of $\Delta_J = 0.03 J$ and $J_2 = 0.19 J$ (Fig. 5 (e) and (f)), the $S = 1/2$ excita-

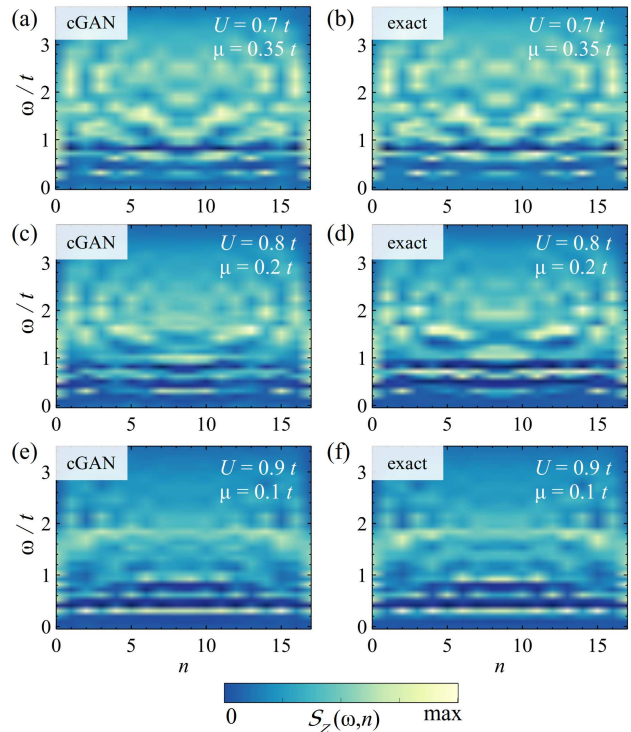


FIG. 6. Real space S^z spin correlators of a one-dimensional Hubbard model of length $n = 18$ generated with the cGAN (a,c,e) in comparison with exact tensor-network calculations (b,d,f). The x-axis labels the site, the y-axis the frequency, and the z-axis the spin correlator in z-direction (Eq. 12). Shown are 3 combinations of the conditional parameters (U, μ) in (a,b), (c,d), and (e,f), as defined in Eq. 11.

tions appear mostly close to the edges at site $n = 0$ and $n = 17$. This behavior is captured well by the generated system in Fig. 5 (e). A stronger first-neighbor dimerization as well as second neighbor exchange interaction (Fig. 5 (a) and Fig. 5 (b)) results in closer lying excitations above the bulk gap at around $0.7 J$. This effect is very accurately captured by the cGAN predictions in Fig. 5 (e)(b). The values of the energy levels, as well as relative magnitudes, are predicted with high accuracy in comparison to the exact tensor-network calculations for all arbitrarily chosen parameter combinations in the defined intervals. The visual accuracy obtained for this model even surpasses the case of the $S = 1/2$ system. This can be related to the spectra themselves which show more pronounced and separated features. To summarize this section, the cGAN is able to simulate the $S = 1$ system with high accuracy almost immediately in the range of the introduced randomness under consideration of the minimal amount of training data, same as in $S = 1/2$.

C. Interacting fermionic systems

We now move on to an interacting model with richer many-body phenomena, in particular incorporating both charge and spin degrees of freedom. The third system we are studying with the cGAN is the doped Hubbard model described by the Hamiltonian

$$\begin{aligned}
H(U, \mu) = & t \sum_{n,s} c_{n,s}^\dagger c_{n+1,s} + \mu \sum_{n,\sigma} c_{n,\sigma}^\dagger c_{n,\sigma} \\
& + U \sum_n (\rho_{n,\uparrow} - 1/2)(\rho_{n,\downarrow} - 1/2) \\
& + \sum_n \xi_n (-1)^n S_n^y,
\end{aligned} \tag{11}$$

where $\rho_{n,s} = c_{n,s}^\dagger c_{n,s}$, $S_n^y = \sum_{s,s'} \sigma_{s,s'}^y c_{n,s}^\dagger c_{n,s'}$, with $\sigma_{s,s'}^y$ the spin Pauli matrix. The previous Hamiltonian is well known to feature a widely rich phase diagram away from half-filling [79] and provides a paradigmatic example of spin-charge separation [80]. In particular, for $\mu = 0$ and $U \gg t$ the electronic system is half-filled, and the spin sector of Eq. 11 maps to a Heisenberg model with an exchange coupling given by $J \sim t^2/U$ for local $S = 1/2$ degrees of freedom. That limit corresponds to the model presented in Eq. 7. However, in the general case away from half-filling, the previous model shows much more complex spin excitation than Eq. 11. The conditional parameters are the onsite Hubbard interaction U , chosen in the interval $U \in [0.5, 1]t$, and $\mu \in [0.0, 0.5]t$ that parametrizes the chemical potential of the system. The randomness is created with an external stagger magnetic field in y -direction with parameter ξ that alternates sign between neighboring sites ($\xi_n \in [0.0, 0.05]t$). We will focus on addressing the many-body spin excitations of this interacting fermionic model, as given by the dynamical spin correlator

$$\begin{aligned}
\mathcal{S}_z(\omega, n) = & \langle GS | S_n^z \delta(\omega - H + E_{GS}) S_n^z | GS \rangle \\
= & \frac{1}{4} \langle GS | (\rho_{n,\uparrow} - \rho_{n,\downarrow}) \delta(H - \omega + E_{GS}) \\
& (\rho_{n,\uparrow} - \rho_{n,\downarrow}) | GS \rangle
\end{aligned} \tag{12}$$

now written with fermionic many-body operators $\rho_{n,s} = c_{n,s}^\dagger c_{n,s}$.

The cGAN learns the mapping $(U, \mu) \rightarrow \mathcal{S}_z(\omega, n)$ and the results are presented in Fig. 6 showing the many-body excitations $\mathcal{S}_z(\omega, n)$ on the corresponding site (x -axis) in the frequency ω range between 0 and $5t$ (y -axis). For the three different combinations of the conditional parameters (U, μ) shown in Fig. 6 (a,b), Fig. 6 (c,d), and Fig. 6 (e,f), the generated spectra of the cGAN Fig. 6 (a,c,e) show very good agreement with the tensor-network calculations Fig. 6 (b,d,f). The variation of the onsite interaction U between $0.7t$ and $0.9t$ as well as the charge occupation varying between $0.1t$ and $0.35t$

does not affect the accuracy of the generated spin excitations. The features and changes of the corresponding parameter combinations, including energy gap as well as location and intensity of states, are all well captured in the simulations of the cGAN.

Considering the results for the three studied many-body systems, we observe that cGANs are able to capture dynamical correlators of one-dimensional systems with high precision. This methodology can easily be extended to different systems without further modifications of the network architecture. The almost instantaneous simulations provide a huge advantage over the numerically costly tensor-network calculations and enable to study the full parameter space of a Hamiltonian without additional computational effort. Despite the relatively small amount of training data (about one magnitude less than for conventional training of GANs as mentioned earlier in this section) the accuracy remains high and the benefits of the cGAN algorithm out-weights the computational costs of creating the training data. As seen in these examples, the cGAN algorithm provides faithful results for substantially different many-body systems, therefore suggesting that this methodology can be readily extended to other many-body systems.

V. HAMILTONIAN INFERENCE AND DATA ASSESSMENT WITH THE GENERATIVE MODEL

In this section, we demonstrate how our conditional generative adversarial model allows us to tackle two additional tasks by exploiting the trained discriminator network as an automatic byproduct of the trained algorithm. The focus of this section is not the generator that was responsible for the generation of the spectra in the previous sections, but the discriminator which is to this point only used during the cGAN training process. The discriminator is trained to distinguish between real, physical systems and unrealistic ones. This feature provides the fundamental ingredient to perform parameter inference and anomaly detection.

A. Hamiltonian learning with the generative model

Here we show how the discriminator network of the generative model allows to directly extract the physical parameters of a certain dynamical correlator. The estimation of physical parameters from data is commonly referred to as Hamiltonian learning and has been explored with a variety of machine learning techniques [81–86]. While these methodologies are usually specifically developed for this purpose, conditional generative algorithms provide this functionality as a direct consequence of their training.

The discriminator learns to assess if a certain dynamical correlator corresponds to the physical parameters

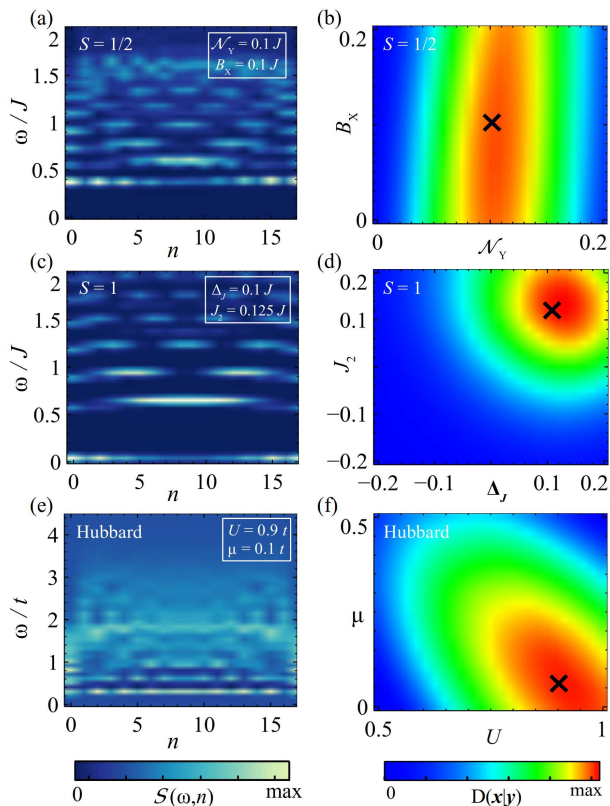


FIG. 7. Hamiltonian learning with the discriminator network of the cGAN for the many-body spectra of a one-dimensional $S = 1/2$ system (a), $S = 1$ -system (c), and the Hubbard model (e). The dynamical correlators $S(\omega, n)$ are defined in Sec. IV. The corresponding predictions of the probabilities of the discriminator, defined as $D(\mathbf{x}|\mathbf{y})$ (see Eq. 2) with \mathbf{x} as input spectra and \mathbf{y} as conditional parameters, are shown in (b,d,f) in a squared scale. The black crosses mark the exact location of the conditional parameters of the input spectra.

given as conditional inputs. Due to instantaneous efficiency, this functionality can be directly applied to inquire the discriminator if a dynamical correlator corresponds to every single possible Hamiltonian. This procedure allows extracting the confidence that the discriminator has for the whole set of parameters as shown in Fig. 7. The probability estimations are shown in Fig. 7 (b), Fig. 7 (d), and Fig. 7 (f) for the three studied many-body systems.

For the $S = 1/2$ many-body dynamical correlator in Fig. 7 (a), the discriminator is able to predict the conditional parameter \mathcal{N}_y with high accuracy, yet yielding a whole range for B_x . This is due to the fact that \mathcal{N}_y has a very strong impact on the dynamical correlator where on the other hand B_x leaves the spectrum almost the same. Therefore, the discriminator detects a strong dependence on \mathcal{N}_y which appears in the exact tensor-network calculations. Interestingly, the consistency of that dynamical correlator with several Hamiltonians simultaneously would represent a challenge for parameter

extraction purely based on supervised learning due to the non-unique parent Hamiltonian [87], representing an advantage of generative-based parameter estimation.

We now move on to the gapped $S = 1$ chain. The parameter predictions for the $S = 1$ spectrum, shown in Fig. 7 (d), provide a single maximum in the parameter assessment, determining the real parameter with good precision. In comparison with the $S = 1/2$, for the $S = 1$ the parameters are uniquely determined by the provided dynamical spin correlator. This enhanced accuracy can also be rationalized from the existence of both bulk and edge excitations, that provide potentially complementary information to the discriminator.

Finally, we move on to the interacting fermionic Hubbard model. The predictions of the Hubbard model, shown in Fig. 7 (f), estimate the area of the exact conditional parameters well and provide a unique maximum for the estimated parameter. In comparison with the $S = 1$ model, the estimated area is larger and less steep, which can be related to the higher complexity of the spectra of the many-body model. In particular, the features of the spectra are not as clear and distinct as it is the case of the $S = 1$ model. Considering that we use the same amount of training data for each many-body system, the differences in accuracy may be related to the higher complexity of the dynamical correlator of the Hubbard model in comparison with the $S = 1$ chain.

For the three considered, models the accuracy of the estimation shows small variations across the different parameter realization and noise level, yet overall giving a good estimation of the vicinity of the exact conditional parameters for each of the studied systems. While we performed here parameter extraction solely with the dynamical correlators, it is worth noting that an analogous procedure can be extended by training a generative model with combined time-dependent [86, 88] or ground state observables [89, 90]. Finally, it is worth noting that while here we focused on simulated dynamical correlators, this procedure can be readily applied with experimentally measured spin excitations [64, 65], providing a procedure for experimental Hamiltonian extraction with conditional generative adversarial networks.

B. Generative model as a many-body assessor

When observing complex phenomena in a quantum system, a key question is if the observed behavior corresponds to the targeted physical state of the system or reflects an undesired artifact of the underlying methodology or setup [91–93]. In particular, many-body calculations often require a degree of controlled accuracy that is model and method-dependent. However, estimating if a certain many-body phenomenon represents a physical system solely from the observation of the dynamical excitations represents an outstanding challenge even for human experts. Here we address how the discriminator provides a direct algorithm to assess if a certain dynamical

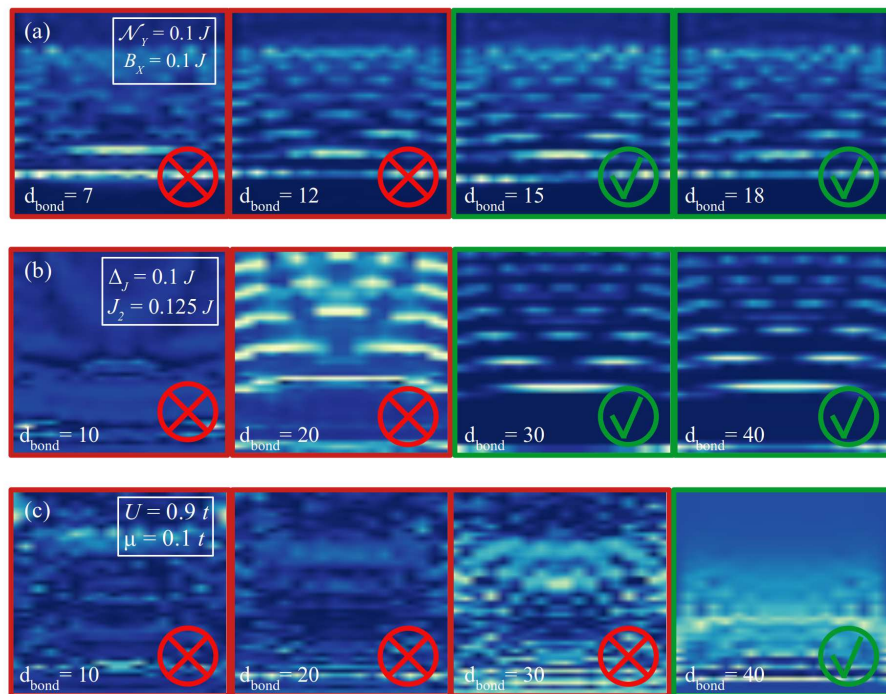


FIG. 8. Outlier detection of faulty unphysical many-body dynamical spectra, emulated by using insufficient bond dimension in tensor-network calculations for the $S = 1/2$ (a), $S = 1$ (b), and Hubbard model (c). The green rectangle marks the bond dimension for which the dynamical correlator is considered as real by the discriminator of the cGAN.

correlator corresponds to a physically-meaningful system, or rather reflects an artifact in the underlying methodology.

The trained discriminator can directly assess if a certain input corresponds to a real result, as a direct consequence of the competitive training with the generator. This procedure provides a discriminator-based outlier detection at no cost after the training of the generative model. To study this effect, we generate different dynamical correlators computed with different degrees of accuracy, which in our tensor-network formalism is directly controlled by the bond dimension of the matrix product state. The discriminator is then used to detect spectra with insufficient accuracy corresponding to ill-converged results. Figure 8 shows the results of the outlier detection for each many-body system. For the $S = 1/2$ system in Figure 8 (a), the discriminator detects outliers for a bond-dimension lower than $d_{\text{bond}} = 15$, for the $S = 1$ system the numerical accuracy becomes insufficient below $d_{\text{bond}} = 30$, and for the Hubbard model, the bond dimension has to be close to $d_{\text{bond}} = 40$, in order to be considered a physically meaningful result by the discriminator. The increasing bond dimension required to pass the discriminator test is a direct consequence of the increasing local Hilbert space of the underlying models and reflects the higher entanglement of the respective many-body states.

It is worth noting that all previous assessment is performed including noisy ξ^α terms in the Hamiltonian,

demonstrating that the generative model distinguishes between physical noise in the Hamiltonian parameters and artifacts stemming from the computational procedure. Furthermore, while in this section we focused on simulated data, an analogous procedure can be extended to experimental data, providing a methodology to assess experimental measurements using generative adversarial learning.

VI. CONCLUSIONS

To summarize, we demonstrated how continuous conditional generative artificial networks allow simulating dynamical correlators for many-body systems which are almost indistinguishable from exact many-body calculations. In stark contrast with conventional supervised algorithms, our methodology allows to simultaneously account for hidden variables unknown to the model, intrinsically account for randomness in the models, reduce by about one order of magnitude the required many-body data required for the training, and exploit the discriminator for Hamiltonian inference and anomaly detection. In particular, we have demonstrated our methodology with three different types of many-body Hamiltonians, starting with a gapless $S = 1/2$ model featuring spinon excitations, an interacting system with topological order and topological boundary modes, and an interacting fermionic system at arbitrary electron fillings. Af-

ter the training process, the cGAN algorithm is able to simulate these systems instantaneous for arbitrary combinations of conditional Hamiltonian parameters. Furthermore, the trained cGAN is not only able to simulate these systems with the generator, the trained discriminator can also be utilized for estimating the parameters of a Hamiltonian from data and for the detection of outliers and wrong-labeled data without the requirement of additional training. These two features can be directly extended with the trained algorithm to data in order to determine unknown underlying Hamiltonians, detect artifacts, and ultimately they can be directly applied to experimental data.

Our results establish a first step towards exploiting generative adversarial machine learning to simulate and design many-body matter. Beyond the results demonstrated here, it is worth noting that the trained cGAN algorithm can be used as a tool in experiments in order to investigate underlying unknown Hamiltonians of systems, either with the generator or discriminator, considering the speed-up for computations of big system sizes and the possibility to simulate Hamiltonians with arbitrary parameters. It is also worth noting that our results use a fully-connected deep neural network for each the generator and discriminator, leaving plenty of room for further future optimizations with deep convolutional neural networks for image compression and feature extraction. Those improvements will allow increasing the accuracy of the cGAN, combining different systems into one single algorithm, and increasing the system size with pre-training on smaller systems which are computationally more feasible to generate.

Acknowledgements: We acknowledge the computational resources provided by the Aalto Science-IT project, and the financial support from the Academy of Finland Projects No. 331342 and No. 336243 and the Jane and Aatos Erkko Foundation. We thank O. Zilberberg, T. Neupert, M. H. Fischer, M. M. Denner, and E. Greplova for useful discussions.

APPENDIX

Appendix A: GAN architecture

For each many-body system of Sec. II we are training a separate cGAN. The explicit network architecture and

training parameters can be found in [58]. In general, we are using fully-connected deep neural networks for the generator and discriminator with a maximal layer dimension of 4048. For the hidden layers, we use the *LeakyRelu* activation function [94]. The output activation function of the discriminator is the *sigmoid* function, and of the generator the output function is the *tanh*-function [11].

Appendix B: Training data generation

For each many-body system, we created 2250 spectra with random conditional parameter combinations. We calculated the dynamical correlators as described in Sec. II B for the many-body Hamiltonians introduced in Sec. IV. In order to minimize the required calculations for the creation of the training set, we are using two methods to enhance the number of examples without doing further tensor-network calculations. First, we are mirroring the 1d systems of 18 sites around site 9 and therefore double the number of systems. Second, we are mimicking the background noise of the random parameters without affecting the conditional parameters. We are changing the intensities depending on the frequency regime by defining a function that adds fluctuations around each energy level seen in the spectra of Sec. IV. The data augmentation function is defined as

$$f(\omega) = \omega [1 + \xi_1 \cos(\xi_2 \omega)] \quad (\text{B1})$$

with random numbers $\xi_1 \in [0.04, 0.1]$ and $\xi_2 = 2\pi * n / 2.5$ with $n \in [1, 4]$. This function adds a different amount of intensity to the dynamical correlator depending on the frequency ω . In an experiment, this procedure would mimic any potential form factor that would affect the intensity of a many-body transition intrinsic to the measurement setup. This method allows adding an arbitrary amount of training examples with the same conditional parameters but with different noise values. In our case, we could enlarge the number of systems from 2250 original tensor-network calculations to 36 000 which represent our full training set. The pre-processing procedure can be found in [58] and consists of a re-scaling of the input spectra between 0 and 1, as well as a separate re-scaling of the conditional parameters.

-
- [1] E. Dagotto, Correlated electrons in high-temperature superconductors, *Rev. Mod. Phys.* **66**, 763 (1994).
 - [2] L. Savary and L. Balents, Quantum spin liquids: a review, *Reports on Progress in Physics* **80**, 016502 (2016).
 - [3] M. R. Norman, Colloquium: Herbertsmithite and the search for the quantum spin liquid, *Rev. Mod. Phys.* **88**, 041002 (2016).
 - [4] S. R. White, Density matrix formulation for quantum renormalization groups, *Phys. Rev. Lett.* **69**, 2863 (1992).
 - [5] G. Carleo and M. Troyer, Solving the quantum many-body problem with artificial neural networks, *Science* **355**, 602 (2017).
 - [6] B.-X. Zheng, C.-M. Chung, P. Corboz, G. Ehlers, M.-P. Qin, R. M. Noack, H. Shi, S. R. White, S. Zhang, and

- G. K.-L. Chan, Stripe order in the underdoped region of the two-dimensional hubbard model, *Science* **358**, 1155 (2017).
- [7] J. P. F. LeBlanc, A. E. Antipov, F. Becca, I. W. Bulik, G. K.-L. Chan, C.-M. Chung, Y. Deng, M. Ferrero, T. M. Henderson, C. A. Jiménez-Hoyos, E. Kozik, X.-W. Liu, A. J. Millis, N. V. Prokof'ev, M. Qin, G. E. Scuseria, H. Shi, B. V. Svistunov, L. F. Tocchio, I. S. Tupitsyn, S. R. White, S. Zhang, B.-X. Zheng, Z. Zhu, and E. Gull (Simons Collaboration on the Many-Electron Problem), Solutions of the two-dimensional hubbard model: Benchmarks and results from a wide range of numerical algorithms, *Phys. Rev. X* **5**, 041041 (2015).
- [8] H. Bin, C. Weihai, W. Xingming, and L. Chunliang, High-Quality Face Image SR Using Conditional Generative Adversarial Networks, arXiv e-prints , arXiv:1707.00737 (2017), [arXiv:1707.00737 \[cs.CV\]](#).
- [9] Y. Gao, R. Singh, and B. Raj, Voice impersonation using generative adversarial networks, in *2018 IEEE International Conference on Acoustics, Speech and Signal Processing (ICASSP)* (IEEE, 2018).
- [10] W. Xiong, W. Luo, L. Ma, W. Liu, and J. Luo, Learning to Generate Time-Lapse Videos Using Multi-Stage Dynamic Generative Adversarial Networks, arXiv e-prints , arXiv:1709.07592 (2017), [arXiv:1709.07592 \[cs.CV\]](#).
- [11] I. Goodfellow, J. Pouget-Abadie, M. Mirza, B. Xu, D. Warde-Farley, S. Ozair, A. Courville, and Y. Bengio, Generative adversarial nets, *Advances in neural information processing systems* **27** (2014).
- [12] P. Isola, J.-Y. Zhu, T. Zhou, and A. A. Efros, Image-to-image translation with conditional adversarial networks, in *2017 IEEE Conference on Computer Vision and Pattern Recognition (CVPR)* (IEEE, 2017).
- [13] A. Lucas, S. López-Tapia, R. Molina, and A. K. Kat-saggelos, Generative adversarial networks and perceptual losses for video super-resolution, *IEEE Transactions on Image Processing* **28**, 3312 (2019).
- [14] J. Nistal, S. Lattner, and G. Richard, DrumGAN: Synthesis of Drum Sounds With Timbral Feature Conditioning Using Generative Adversarial Networks, arXiv e-prints , arXiv:2008.12073 (2020), [arXiv:2008.12073 \[eess.AS\]](#).
- [15] J. Carrasquilla and R. G. Melko, Machine learning phases of matter, *Nature Physics* **13**, 431 (2017).
- [16] J. Carrasquilla, Machine learning for quantum matter, *Advances in Physics: X* **5**, 1797528 (2020).
- [17] G. Carleo, I. Cirac, K. Cranmer, L. Daudet, M. Schuld, N. Tishby, L. Vogt-Maranto, and L. Zdeborová, Machine learning and the physical sciences, *Rev. Mod. Phys.* **91**, 045002 (2019).
- [18] K. Ch'ng, J. Carrasquilla, R. G. Melko, and E. Khatami, Machine learning phases of strongly correlated fermions, *Phys. Rev. X* **7**, 031038 (2017).
- [19] E. P. L. van Nieuwenburg, Y.-H. Liu, and S. D. Huber, Learning phase transitions by confusion, *Nature Physics* **13**, 435 (2017).
- [20] G. Torlai, B. Timar, E. P. L. van Nieuwenburg, H. Levine, A. Omran, A. Keesling, H. Bernien, M. Greiner, V. Vuletić, M. D. Lukin, R. G. Melko, and M. Endres, Integrating neural networks with a quantum simulator for state reconstruction, *Phys. Rev. Lett.* **123**, 230504 (2019).
- [21] P. M. Vecsei, K. Choo, J. Chang, and T. Neupert, Neural network based classification of crystal symmetries from x-ray diffraction patterns, *Phys. Rev. B* **99**, 245120 (2019).
- [22] E. Greplova, A. Valenti, G. Boschung, F. Schäfer, N. Lörch, and S. D. Huber, Unsupervised identification of topological phase transitions using predictive models, *New Journal of Physics* **22**, 045003 (2020).
- [23] E. van Nieuwenburg, E. Bairey, and G. Refael, Learning phase transitions from dynamics, *Phys. Rev. B* **98**, 060301 (2018).
- [24] D. Carvalho, N. A. García-Martínez, J. L. Lado, and J. Fernández-Rossier, Real-space mapping of topological invariants using artificial neural networks, *Phys. Rev. B* **97**, 115453 (2018).
- [25] E. Greplova, C. Kraglund Andersen, and K. Mølmer, Quantum parameter estimation with a neural network, arXiv e-prints , arXiv:1711.05238 (2017), [arXiv:1711.05238 \[quant-ph\]](#).
- [26] J. F. Rodríguez-Nieva and M. S. Scheurer, Identifying topological order through unsupervised machine learning, *Nature Physics* **15**, 790 (2019).
- [27] M. S. Scheurer and R.-J. Slager, Unsupervised machine learning and band topology, *Phys. Rev. Lett.* **124**, 226401 (2020).
- [28] M. Kenig and Y. Lahini, Tunable Realizations of Correlated Quantum Walks using an Unsupervised Generative Model, arXiv e-prints , arXiv:2110.06911 (2021), [arXiv:2110.06911 \[quant-ph\]](#).
- [29] Z. Liu, S. P. Rodrigues, and W. Cai, Simulating the Ising Model with a Deep Convolutional Generative Adversarial Network, arXiv e-prints , arXiv:1710.04987 (2017), [arXiv:1710.04987 \[cond-mat.dis-nn\]](#).
- [30] S. Ahmed, C. S. Muñoz, F. Nori, and A. F. Kockum, Quantum state tomography with conditional generative adversarial networks, *Physical Review Letters* **127**, 10.1103/physrevlett.127.140502 (2021).
- [31] A. Radford, L. Metz, and S. Chintala, Unsupervised Representation Learning with Deep Convolutional Generative Adversarial Networks, arXiv e-prints , arXiv:1511.06434 (2015), [arXiv:1511.06434 \[cs.LG\]](#).
- [32] G. Perarnau, J. van de Weijer, B. Raducanu, and J. M. Álvarez, Invertible Conditional GANs for image editing, arXiv e-prints , arXiv:1611.06355 (2016), [arXiv:1611.06355 \[cs.CV\]](#).
- [33] T. Salimans, I. Goodfellow, W. Zaremba, V. Cheung, A. Radford, and X. Chen, Improved Techniques for Training GANs, arXiv e-prints , arXiv:1606.03498 (2016), [arXiv:1606.03498 \[cs.LG\]](#).
- [34] J. Gui, Z. Sun, Y. Wen, D. Tao, and J. Ye, A Review on Generative Adversarial Networks: Algorithms, Theory, and Applications, arXiv e-prints , arXiv:2001.06937 (2020), [arXiv:2001.06937 \[cs.LG\]](#).
- [35] T. Karras, T. Aila, S. Laine, and J. Lehtinen, Progressive Growing of GANs for Improved Quality, Stability, and Variation, arXiv e-prints , arXiv:1710.10196 (2017), [arXiv:1710.10196 \[cs.NE\]](#).
- [36] A. Brock, J. Donahue, and K. Simonyan, Large scale GAN training for high fidelity natural image synthesis, in *7th International Conference on Learning Representations, ICLR 2019, New Orleans, LA, USA, May 6-9, 2019* (OpenReview.net, 2019).
- [37] M. Mirza and S. Osindero, Conditional Generative Adversarial Nets, arXiv e-prints , arXiv:1411.1784 (2014), [arXiv:1411.1784 \[cs.LG\]](#).

- [38] G. Antipov, M. Baccouche, and J.-L. Dugelay, Face Aging With Conditional Generative Adversarial Networks, arXiv e-prints, arXiv:1702.01983 (2017), [arXiv:1702.01983](https://arxiv.org/abs/1702.01983) [cs.CV].
- [39] H. Zhang, V. Sindagi, and V. M. Patel, Image De-raining Using a Conditional Generative Adversarial Network, arXiv e-prints, arXiv:1701.05957 (2017), [arXiv:1701.05957](https://arxiv.org/abs/1701.05957) [cs.CV].
- [40] L. de Oliveira, M. Paganini, and B. Nachman, Learning particle physics by example: Location-aware generative adversarial networks for physics synthesis, *Computing and Software for Big Science* **1**, [10.1007/s41781-017-0004-6](https://doi.org/10.1007/s41781-017-0004-6) (2017).
- [41] M. Paganini, L. de Oliveira, and B. Nachman, Accelerating science with generative adversarial networks: An application to 3d particle showers in multilayer calorimeters, *Physical Review Letters* **120**, [10.1103/physrevlett.120.042003](https://doi.org/10.1103/physrevlett.120.042003) (2018).
- [42] N. Perraudin, S. Marcon, A. Lucchi, and T. Kacprzak, Emulation of cosmological mass maps with conditional generative adversarial networks, *Frontiers in Artificial Intelligence* **4**, [10.3389/frai.2021.673062](https://doi.org/10.3389/frai.2021.673062) (2021).
- [43] A. Weiße, G. Wellein, A. Alvermann, and H. Fehske, The kernel polynomial method, *Rev. Mod. Phys.* **78**, 275 (2006).
- [44] F. A. Wolf, I. P. McCulloch, O. Parcollet, and U. Schollwöck, Chebyshev matrix product state impurity solver for dynamical mean-field theory, *Phys. Rev. B* **90**, 115124 (2014).
- [45] J. L. Lado and M. Sigrist, Solitonic in-gap modes in a superconductor-quantum antiferromagnet interface, *Phys. Rev. Research* **2**, 023347 (2020).
- [46] M. Ganahl, P. Thunström, F. Verstraete, K. Held, and H. G. Evertz, Chebyshev expansion for impurity models using matrix product states, *Phys. Rev. B* **90**, 045144 (2014).
- [47] V. Kaskela and J. L. Lado, Dynamical topological excitations in parafermion chains, *Phys. Rev. Research* **3**, 013095 (2021).
- [48] J. L. Lado and O. Zilberberg, Topological spin excitations in harper-heisenberg spin chains, *Phys. Rev. Research* **1**, 033009 (2019).
- [49] M. Rösner and J. L. Lado, Inducing a many-body topological state of matter through coulomb-engineered local interactions, *Phys. Rev. Research* **3**, 013265 (2021).
- [50] R. Koch and J. L. Lado, Neural network enhanced hybrid quantum many-body dynamical distributions, *Phys. Rev. Research* **3**, 033102 (2021).
- [51] M. Fishman, S. R. White, and E. Miles Stoudenmire, The ITensor Software Library for Tensor Network Calculations, arXiv e-prints, arXiv:2007.14822 (2020), [arXiv:2007.14822](https://arxiv.org/abs/2007.14822) [cs.MS].
- [52] ITensor Library <http://itensor.org>.
- [53] DMRGpy Library <https://github.com/joselado/dmrgpy>.
- [54] D. Jackson, On approximation by trigonometric sums and polynomials, *Transactions of the American Mathematical Society* **13**, 491 (1912).
- [55] D. Hendry, H. Chen, P. Weinberg, and A. E. Feiguin, Chebyshev expansion of spectral functions using restricted boltzmann machines, *Phys. Rev. B* **104**, 205130 (2021).
- [56] This enhancement procedure is not critical for a simple single-particle system but becomes significantly more important for the computational costly many-body systems studied in the next section.
- [57] L. Deng, The mnist database of handwritten digit images for machine learning research, *IEEE Signal Processing Magazine* **29**, 141 (2012).
- [58] The code for each cGAN can be found in [github-rouvenkoch](https://github.com/rouvenkoch).
- [59] L. D. Faddeev and L. A. Takhtadzhyan, Spectrum and scattering of excitations in the one-dimensional isotropic heisenberg model, *Journal of Soviet Mathematics* **24**, 241 (1984).
- [60] T. Giamarchi, *Quantum Physics in One Dimension* (Oxford University Press, 2003).
- [61] H. Bethe, Zur theorie der metalle, *Zeitschrift fur Physik* **71**, 205 (1931).
- [62] D.-J. Choi, N. Lorente, J. Wiebe, K. von Bergmann, A. F. Otte, and A. J. Heinrich, Colloquium: Atomic spin chains on surfaces, *Rev. Mod. Phys.* **91**, 041001 (2019).
- [63] A. J. Heinrich, J. A. Gupta, C. P. Lutz, and D. M. Eigler, Single-atom spin-flip spectroscopy, *Science* **306**, 466 (2004).
- [64] A. Spinelli, B. Bryant, F. Delgado, J. Fernández-Rossier, and A. F. Otte, Imaging of spin waves in atomically designed nanomagnets, *Nature Materials* **13**, 782 (2014).
- [65] R. Toskovic, R. van den Berg, A. Spinelli, I. S. Eliens, B. van den Toorn, B. Bryant, J.-S. Caux, and A. F. Otte, Atomic spin-chain realization of a model for quantum criticality, *Nature Physics* **12**, 656 (2016).
- [66] S. Baumann, W. Paul, T. Choi, C. P. Lutz, A. Ardavan, and A. J. Heinrich, Electron paramagnetic resonance of individual atoms on a surface, *Science* **350**, 417 (2015).
- [67] K. Yang, Y. Bae, W. Paul, F. D. Natterer, P. Willke, J. L. Lado, A. Ferrón, T. Choi, J. Fernández-Rossier, A. J. Heinrich, and C. P. Lutz, Engineering the eigenstates of coupled spin-1/2 atoms on a surface, *Phys. Rev. Lett.* **119**, 227206 (2017).
- [68] P. Willke, A. Singha, X. Zhang, T. Esat, C. P. Lutz, A. J. Heinrich, and T. Choi, Tuning single-atom electron spin resonance in a vector magnetic field, *Nano Letters* **19**, 8201 (2019).
- [69] K. Yang, W. Paul, S.-H. Phark, P. Willke, Y. Bae, T. Choi, T. Esat, A. Ardavan, A. J. Heinrich, and C. P. Lutz, Coherent spin manipulation of individual atoms on a surface, *Science* **366**, 509 (2019).
- [70] K. Yang, S.-H. Phark, Y. Bae, T. Esat, P. Willke, A. Ardavan, A. J. Heinrich, and C. P. Lutz, Probing resonating valence bond states in artificial quantum magnets, *Nature Communications* **12**, [10.1038/s41467-021-21274-5](https://doi.org/10.1038/s41467-021-21274-5) (2021).
- [71] I. Affleck, T. Kennedy, E. H. Lieb, and H. Tasaki, Rigorous results on valence-bond ground states in antiferromagnets, *Phys. Rev. Lett.* **59**, 799 (1987).
- [72] F. D. M. Haldane, Nonlinear field theory of large-spin heisenberg antiferromagnets: Semiclassically quantized solitons of the one-dimensional easy-axis néel state, *Phys. Rev. Lett.* **50**, 1153 (1983).
- [73] F. Pollmann, A. M. Turner, E. Berg, and M. Oshikawa, Entanglement spectrum of a topological phase in one dimension, *Phys. Rev. B* **81**, 064439 (2010).
- [74] Z.-C. Gu and X.-G. Wen, Tensor-entanglement-filtering renormalization approach and symmetry-protected topological order, *Phys. Rev. B* **80**, 155131 (2009).
- [75] F. Pollmann, E. Berg, A. M. Turner, and M. Oshikawa, Symmetry protection of topological phases in one-dimensional quantum spin systems, *Phys. Rev. B* **85**,

- 075125 (2012).
- [76] X. Chen, Z.-C. Gu, and X.-G. Wen, Classification of gapped symmetric phases in one-dimensional spin systems, *Phys. Rev. B* **83**, 035107 (2011).
- [77] G. Xu, J. F. DiTusa, T. Ito, K. Oka, H. Takagi, C. Broholm, and G. Aeppli, $\gamma_2\text{BaNiO}_5$: A nearly ideal realization of the $s = 1$ heisenberg chain with antiferromagnetic interactions, *Phys. Rev. B* **54**, R6827 (1996).
- [78] S. Mishra, G. Catarina, F. Wu, R. Ortiz, D. Jacob, K. Eimre, J. Ma, C. A. Pignedoli, X. Feng, P. Ruffieux, J. Fernández-Rossier, and R. Fasel, Observation of fractional edge excitations in nanographene spin chains, *Nature* **598**, 287 (2021).
- [79] F. H. L. Essler, H. Frahm, F. Göhmann, A. Klümper, and V. E. Korepin, *The One-Dimensional Hubbard Model* (Cambridge University Press, 2005).
- [80] J. Voit, One-dimensional fermi liquids, *Reports on Progress in Physics* **58**, 977 (1995).
- [81] N. Wiebe, C. Granade, C. Ferrie, and D. G. Cory, Hamiltonian learning and certification using quantum resources, *Phys. Rev. Lett.* **112**, 190501 (2014).
- [82] N. Wiebe, C. Granade, C. Ferrie, and D. Cory, Quantum hamiltonian learning using imperfect quantum resources, *Phys. Rev. A* **89**, 042314 (2014).
- [83] J. Wang, S. Paesani, R. Santagati, S. Knauer, A. A. Gentile, N. Wiebe, M. Petruzzella, J. L. O'Brien, J. G. Rarity, A. Laing, and M. G. Thompson, Experimental quantum hamiltonian learning, *Nature Physics* **13**, 551 (2017).
- [84] Z. Li, L. Zou, and T. H. Hsieh, Hamiltonian tomography via quantum quench, *Phys. Rev. Lett.* **124**, 160502 (2020).
- [85] A. Valenti, E. van Nieuwenburg, S. Huber, and E. Greplova, Hamiltonian learning for quantum error correction, *Phys. Rev. Research* **1**, 033092 (2019).
- [86] A. Valenti, G. Jin, J. Léonard, S. D. Huber, and E. Greplova, Scalable Hamiltonian learning for large-scale out-of-equilibrium quantum dynamics, arXiv e-prints , arXiv:2103.01240 (2021), arXiv:2103.01240 [quant-ph].
- [87] C. Cao, S.-Y. Hou, N. Cao, and B. Zeng, Supervised learning in hamiltonian reconstruction from local measurements on eigenstates, *Journal of Physics: Condensed Matter* **33**, 064002 (2020).
- [88] A. Bohrdt, S. Kim, A. Lukin, M. Rispoli, R. Schittko, M. Knap, M. Greiner, and J. Léonard, Analyzing nonequilibrium quantum states through snapshots with artificial neural networks, *Phys. Rev. Lett.* **127**, 150504 (2021).
- [89] J. R. Garrison and T. Grover, Does a single eigenstate encode the full hamiltonian?, *Phys. Rev. X* **8**, 021026 (2018).
- [90] E. Chertkov and B. K. Clark, Computational inverse method for constructing spaces of quantum models from wave functions, *Phys. Rev. X* **8**, 031029 (2018).
- [91] I. Convy, H. Liao, S. Zhang, S. Patel, W. P. Livingston, H. N. Nguyen, I. Siddiqi, and K. B. Whaley, Machine Learning for Continuous Quantum Error Correction on Superconducting Qubits, arXiv e-prints , arXiv:2110.10378 (2021), arXiv:2110.10378 [quant-ph].
- [92] P. Baireuther, T. E. O'Brien, B. Tarasinski, and C. W. J. Beenakker, Machine-learning-assisted correction of correlated qubit errors in a topological code, *Quantum* **2**, 48 (2018).
- [93] P. Baireuther, M. D. Caio, B. Criger, C. W. J. Beenakker, and T. E. O'Brien, Neural network decoder for topological color codes with circuit level noise, *New Journal of Physics* **21**, 013003 (2019).
- [94] A. L. Maas, Rectifier nonlinearities improve neural network acoustic models (2013).